Incommensurate antiferromagnetism in a pure spin system via cooperative organization of local and itinerant moments

Yejun Feng[a,b,1], Jiyang Wang[b], D. M. Silevitch[b], B. Mihaila[c], J. W. Kim[a], J.-Q. Yan[d,e], R. K. Schulze[c], Nayoon Woo[b], A. Palmer[b], Y. Ren[a], Jasper van Wezel[f,2], P. B. Littlewood[b,g], and T. F. Rosenbaum[b,1]

[a]The Advanced Photon Source, Argonne National Laboratory, Argonne, IL 60439; [b]The James Franck Institute and Department of Physics, The University of Chicago, Chicago, IL 60637; [c]Materials Science and Technology Division, Los Alamos National Laboratory, Los Alamos, NM 87545; [d]Department of Materials Science and Engineering, University of Tennessee, Knoxville, TN 37996; [e]Materials Science and Technology Division, Oak Ridge National Laboratory, Oak Ridge, TN 37831; [f]Materials Science Division, Argonne National Laboratory, Argonne, IL 60439; and [g]Physical Sciences and Engineering, Argonne National Laboratory, Argonne, IL 60439

Edited by Susan N. Coppersmith, University of Wisconsin, Madison, WI, and approved January 17, 2013 (received for review October 4, 2012)

Materials with strong correlations are prone to spin and charge instabilities, driven by Coulomb, magnetic, and lattice interactions. In materials that have significant localized and itinerant spins, it is not obvious which will induce order. We combine electrical transport, X-ray magnetic diffraction, and photoemission studies with band structure calculations to characterize successive antiferromagnetic transitions in GdSi. GdSi has both sizable local moments and a partially nested Fermi surface, without confounding contributions from orbital effects. We identify a route to incommensurate order where neither type of moment dominates, but is rooted in cooperative feedback between them. The nested Fermi surface of the itinerant electrons induces strong interactions between local moments at the nesting vector, whereas the ordered local moments in turn provide the necessary coupling for a spin-density wave to form among the itinerant electrons. This mechanism echoes the cooperative interactions between electrons and ions in charge-density–wave materials, and should be germane across a spectrum of transition-metal and rare-earth intermetallic compounds.

itinerant magnetism | RKKY interaction | asymmetric line shape

Incommensurate density waves emerge in a wide variety of correlated electron systems. They are a common aspect in cuprate superconductors (1, 2), itinerant transition-metal magnets (3, 4), and rare-earth compounds (5–7), as well as low-dimensional charge-ordered materials (8, 9) and perovskite manganites (10, 11). In contrast with commensurate density waves, the incommensurate states are often electronically soft (11), and many spin and charge orders in metals are continuously tunable (9, 12). Furthermore, the incommensurate structures are often only weakly coupled to other degrees of freedom in the underlying lattice, giving rise to the rare possibility of direct theoretical modeling of a variety of experimentally accessible material systems, spanning from functional materials of technological importance (10, 11) to fundamental topics of emergent states in quantum critical phenomena (9, 12).

Spin states with long-range incommensurate magnetic order may be stabilized by itinerant electrons through two distinct mechanisms. If the Fermi surface has well-nested regions, the itinerant electrons themselves typically become unstable toward the formation of a spin-density wave (SDW) (13). A prominent example of this class of materials is elemental chromium (4, 13, 14). Alternatively, in the presence of local magnetic moments, the itinerant electrons may form screening clouds which mediate magnetic interactions between the local moments and cause them to order through the Ruderman–Kittel–Kasuya–Yosida (RKKY) exchange interaction (5, 15).

To form a nesting-driven SDW or charge-density wave (CDW) (13), it is necessary to have a nonzero coupling between itinerant electron states on opposing portions of the nested Fermi surface. In the presence of a perfectly nested Fermi surface, the required coupling strength may be infinitesimally small, but in real materials one must always have a finite coupling strength because perfect nesting never occurs in more than one dimension. In the case of CDWs, this coupling is normally provided by phonons, because electrons can transition between nested states by scattering off lattice distortions. For SDWs in the presence of nearly perfect nesting conditions, such as in elemental Cr, phonon scattering may provide a similar coupling term (13). More generally, however, alternative mechanisms may dominate the coupling between nested states. As we point out here for the particular case of GdSi, one mechanism that is not often discussed (16, 17) is that the interaction between itinerant spins and local moments may provide the necessary coupling strength between nested portions of the Fermi surface and let itinerant electron spins form a SDW. At the same time, the maximum in the susceptibility of those itinerant electrons, which results from nesting, influences the RKKY interactions between local moments so that they will tend to order at the same wave vector of the itinerant SDW. The Fermi surface nesting condition restricts the typically broad q dependence of the RKKY interaction, and determines the magnetic ordering wave vector for both itinerant and local moments. Thus, not only can RKKY interaction and nesting coexist but can even cooperate in the formation of incommensurate spin order involving both local moments and itinerant electron states.

Incommensurate spin structures built from local moments are frequently observed in rare-earth elements and compounds, although not often as the ground state. For elemental rare-earth systems such as Tb, Dy, Ho, Er, and Tm, antiferromagnetic helical or spiral spin structures exist at elevated temperatures with a strong spin–orbit coupling typically driving a low-temperature transition to either ferromagnetic or commensurate spin ordering (5). Among the rare-earth elements, Gd is unique in that the electrons in the 4*f* shell combine to possess only spin but no orbital component under Hund's rules. Thus, Gd compounds are often ideal choices for studies of collective spin behavior, such as, for example, the frustrated antiferromagnetic gadolinium gallium garnet, GGG (18). Studying the spin behavior in Gd compounds via neutron scattering is difficult due to the large neutron absorption cross-section of the most common isotope. However, long-range incommensurate spin ordering was revealed

Author contributions: Y.F. and T.F.R. designed research; Y.F., J.W., D.M.S., B.M., J.W.K., R.K.S., N.W., A.P., Y.R., J.v.W., and P.B.L. performed research; J.-Q.Y. contributed new reagents/analytic tools; Y.F., D.M.S., and T.F.R. analyzed data; and Y.F., D.M.S., J.v.W., and T.F.R. wrote the paper.

The authors declare no conflict of interest.

This article is a PNAS Direct Submission.

[1]To whom correspondence may be addressed. E-mail: yejun@aps.anl.gov or t-rosenbaum@uchicago.edu.

[2]Present address: H. H. Wills Physics Laboratory, University of Bristol, Bristol BS8 1TL, United Kingdom.

This article contains supporting information online at www.pnas.org/lookup/suppl/doi:10.1073/pnas.1217292110/-/DCSupplemental.

by X-ray magnetic diffraction in several Gd compounds such as $GdCo_2Ge_2$, $GdNi_2Ge_2$, and $GdNi_2B_2C$ (6, 7, 19), and the idea of cooperative RKKY and nesting effects was discussed in systems such as $GdNi_2Ge_2$ (19) and Tb_2PdSi_3 (20). However, for $GdNi_2Ge_2$ and $GdNi_2B_2C$, lack of a resistance anomaly at the onset of magnetic ordering suggests that the incommensurate spin structure is not likely to involve any gapping of the Fermi surface (21, 22), and for Tb_2PdSi_3 it is unclear whether resolution-limited, long-range magnetic order exists at the wave vector suggested by the angle-resolved photoemission spectroscopy (ARPES) work (20).

Here we focus on the binary intermetallic GdSi (Fig. 1*A*), which is antiferromagnetic below 55 K (23, 24). Our X-ray measurements indicate that GdSi possesses an incommensurate spin structure in the ground state, involving both large local moments and itinerant electron spins. Longitudinal resistivity and Hall coefficient data suggest that the magnetic transition is accompanied by a sizable change of the Fermi surface with a reduction of density of states (DOS) and opening of a band gap, which is also confirmed by photoemission measurements and *ab initio* band structure calculations. The sheet-like nature of the Fermi surface for the gapped states and the corresponding necessary presence of nesting are evidenced by the diffraction line shape at the incipience of antiferromagnetic order, where the resonance-enhanced static magnetic form factor closely mimics the imaginary part of the itinerant spin susceptibility. This strongly suggests that the magnetic ground state in GdSi involves a cooperative ordering mechanism, in which itinerant electrons mediate RKKY interactions that tend to order the local moments, whereas the local moments in turn provide the necessary coupling strength between nested itinerant states to form a SDW. This situation is intriguingly similar to the phonon-mediated nesting instability in CDWs, which consist of simultaneously ordered modulations in the density of itinerant electrons and in the displacements of local ionic cores (25).

Results

Lattice and Incommensurate Magnetic Structures. The broad temperature evolution of the magnetic susceptibility of GdSi (Fig. 1*B*, *Inset*) is consistent with what has been previously reported in the literature (24). Here, we focus on the detailed region around T_N (Fig. 1*B*). In contrast with the single transition reported in the literature, we observed two anomalies at 53.0 and 54.7 K along all three principal axes. The anomalies point to two magnetic transitions, from paramagnet to antiferromagnet at $T_N = 54.7$ K, followed by a spin–flip transition at $T_{SF} = 53.0$ K. From 53 K to our base temperature of 1.8 K the susceptibilities vary smoothly, with no signatures of additional phase transitions.

GdSi in the paramagnetic state has an orthorhombic structure with a space group Pnma (no. 63) (26). Gd ions sit on the 4*c* site, with the only local symmetry a mirror plane about the *b* axis. Our high-resolution X-ray diffraction results indicate that in the magnetic phase, the mosaic profile of lattice diffraction orders involving both nonzero K and L indices shows spontaneous twinning of the single crystal and a symmetry reduction in the lattice. Longitudinal θ–2θ scans of individual mosaic peaks show clear splitting of the d-spacing related to general orders such as (1, 1, 1) and (0, 3, 3) (Fig. 2*A*). The twofold splitting of (1, 1, 1) order indicates that GdSi has a monoclinic structure in the antiferromagnetic phase instead of triclinic. The difference between (0, 3, 3) and (0, 3, −3) orders gives $\alpha = 89.916° \pm 0.002°$ between the b^* and c^* axes at $T = 4$ K, consistent with the splitting of the (1, 1, 1) order. Although the d-spacing splitting drops below instrumental resolution near the phase boundary, the curvature of its temperature dependence suggests that the symmetry reduction happens at T_{SF} rather than T_N. This is further corroborated by magnetic diffraction results (discussed below) that reveal a weak first-order phase transition at T_{SF}. The space group of the lattice structure in the lower antiferromagnetic phase was determined at 6.6 K using high-resolution X-ray powder diffraction as $P2_1/c$ (no. 14). In addition, the b-axis lattice constant slightly expands upon cooling through T_N, indicating an overall magnetostrictive effect.

Using resonant X-ray magnetic diffraction, we identified the characteristic incommensurate wave vectors as $Q = (0, q_b, q_c) \sim (0, 0.483, 0.092)$ in both antiferromagnetic phases. Between T_{SF} and T_N, the orthorhombic lattice structure supports two degenerate magnetic domains along the $(0, \pm q_b, q_c)$ directions, related by a mirror symmetry about the (0, 1, 0) plane. Below T_{SF}, the monoclinic symmetry breaks the twofold magnetic degeneracy in the b–c plane, and each magnetic order $(0, q_b, q_c)$ becomes associated exclusively with the corresponding lattice domain. The magnetic nature of the incommensurate order is shown by the resonance energy dependence across the Gd $L2$ edge (7,930 eV) in the σ–π diffraction geometry (Fig. 3*A*), indicating an electric dipole ($E1$)-dominated resonance behavior between Gd $2p_{1/2}$–$5d_{3/2}$ states (27).

Azimuthal scans of the magnetic order at the resonant condition provide detailed knowledge about the antiferromagnetic spin structure (27). Defining the azimuthal angle $\varphi = 0$ when the (0, 0, 1) order is within the diffraction plane, azimuthal scans about $(0, 2\pm q_b, \pm q_c)$ are plotted in Fig. 2*B*. In the high-temperature phase between T_N and T_{SF}, the diffraction intensity reaches zero at certain φ values, a signature of a collinear spin structure (27). Fitting our data with a collinear spin arrangement that is precessing around the diffraction wave vector $(0, 2-q_b, -q_c)$, we find that the spin structure lies within the b–c plane, transverse to the incommensurate wave vector $Q = (0, q_b, q_c)$. As the Q vector tilts by only about 9° away from the b axis, the predominant projection of the spin moments lies along c. This is consistent with the susceptibility results shown in Fig. 1*B*. Between T_N and T_{SF}, susceptibility curves along a and b have similar shapes and are stronger than along c, indicating that a and b are soft axes with magnetic moments aligned nearly perpendicular to them. We note that the a- and c-axis susceptibilities become similar in shape below T_{SF} and are also much smaller than that of the b axis (Fig. 1*B*, *Inset*), indicating that the spin structure becomes noncollinear (planar) and lies close to the

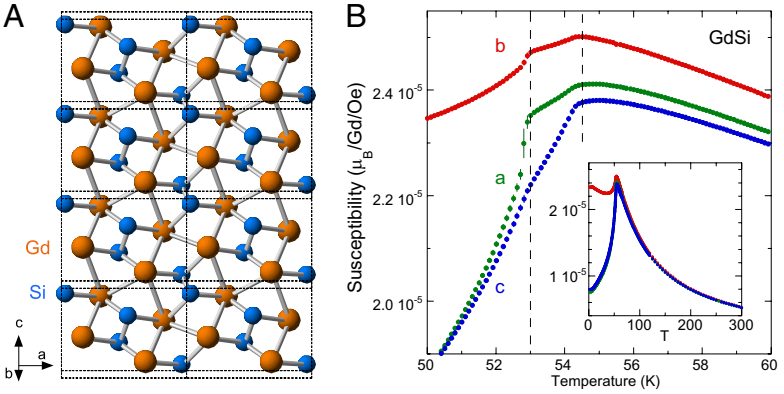

Fig. 1. (*A*) Lattice structure of GdSi, viewed along the incommensurate antiferromagnetic wave vector (0, 0.483, 0.092) direction. (*B*) DC magnetic susceptibility measured along all three orthogonal axes shows two magnetic phase transitions at 53.0 and 54.7 K. (*Inset*) Susceptibility vs. temperature from 1.8 to 300 K.

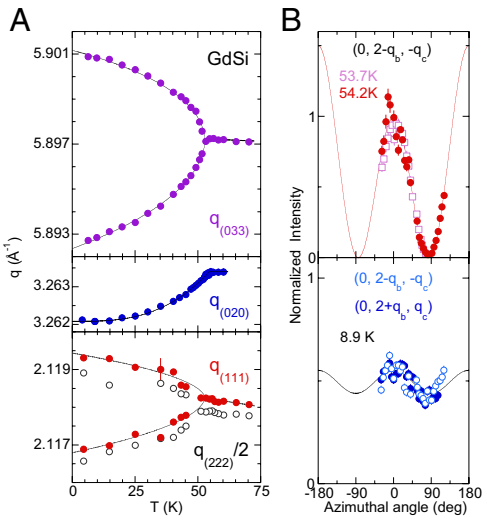

Fig. 2. Lattice and magnetic structures of GdSi. (*A*) Lattice symmetry reduction is shown by *q* values of orders (0, 3, 3), (0, 2, 0), (1, 1, 1), and (2, 2, 2) evolving in the magnetic phase. (*B*) Azimuthal dependence of the antiferromagnetic diffraction intensity in both magnetic phases.

a–*c* plane. This is reflected in a relatively weak azimuthal angle dependence shown in Fig. 2*B* (*Lower*). Although the low-temperature azimuthal response also could be consistent with spins aligned along *b*, the magnetic susceptibility rules out this possibility.

Measurements of *q* values of both (0, $2\pm q_b$, $\pm q_c$) orders (Fig. 3*B*) show that the magnetic wave vector Q evolves smoothly with temperature until a discontinuous jump at T_{SF}, indicative of a first-order spin–flip transition. We also plot in Fig. 3*C* the evolution of (0, q_b, q_c) in reciprocal space as a function of temperature, with individual components of q_b and q_c calculated from $q^2_{(0,\,2\pm q_b,\,\pm q_c)} = q_c^2 + (q_{(020)} \pm q_b)^2$. Both antiferromagnetic phases are incommensurate from 54.5 to 4.0 K.

The first-order jump of the incommensurate wave vector at T_{SF} allows one to trace both magnetic order parameters separately even at azimuthal angle $\varphi = 0$ (Fig. 3*D*). We notice that although the spin–flip transition at T_{SF} is first order, the transition from paramagnetic to incommensurate antiferromagnetic phase at T_N is likely to be second order.

Fermi Surface Gapping at the Antiferromagnetic Transition. The incipient incommensurate magnetic order in GdSi is accompanied by changes at the Fermi surface. Here, the behavior of itinerant electrons at the magnetic transition is evidenced experimentally by both electrical resistivity and Hall coefficient measurements, and further corroborated by DOS calculations. All results point to the creation of a Fermi surface gap inside the antiferromagnetic phase. The resistivity shown in Fig. 4*A* for $T >> T_N$ exhibits a slow decrease in $\rho(T)$ and hence a large projected residual resistivity, ρ_0. Such behavior is naturally assigned to strong scattering between the charge carriers and the disordered local moments. In such a case, one would expect that the onset of magnetic order would lead to a reduction in the resistivity, as electron backscattering from magnetic fluctuations is suppressed. Instead, we see that below T_N the resistivity abruptly increases along all three major axes (Fig. 4 *B*–*D*), consistent with the opening of a gap (as in CDW systems), but then decreases at low temperatures to a value of 2–3 μΩ·cm, more than 1 order of magnitude smaller than the projected ρ_0. Furthermore, a precursor of the rising anomaly in $\rho(T)$ is observed in ρ_{bb} as high as 15 K above T_N, which is consistent with a transient gap due to dynamic fluctuations of incipient order and has been observed in many correlated electron systems straddling the weak and strong coupling limits (28). We thus infer that magnetic order (with a substantial moment) is accompanied by strong Fermi surface reconstruction.

Further evidence for Fermi surface reconstruction emerges from the Hall coefficient $R_H(T)$, measured under different current/field configurations (Fig. 4*E*). Above T_N, R_H has opposite signs along two different directions, indicating that the paramagnetic Fermi surface must possess open orbits along some directions, and also likely multiple bands. As the magnetic ordering temperature is crossed, R_H for $H||c$ and $I||a$ experiences a large change in magnitude and ultimately changes sign. Given the multiband nature of the system, this is likely to indicate significant removal of DOS at the Fermi surface upon the magnetic ordering, leaving only small patches of hole character below T_N. Similarly, drastic removals of DOS with associated sign changes in R_H was observed at the CDW transitions in $NbSe_2$ (8) and α–U (29).

To correlate the magnetic and transport measurements with the electronic structure, we study the DOS of GdSi at the Fermi surface by collecting UV photoemission spectra and comparing them to electronic structure calculations. In the paramagnetic phase, the DOS is directly measured by photoemission, with several peak features in the valence bands identified in Fig. 5*A*. Specifically, we note that right at the Fermi surface there is a significant accumulation of spectral weight. With the first-principles calculation of the DOS in the antiferromagnetic state, we note that most spectral features in the photoemission data are faithfully reproduced away from the Fermi surface (vertical bars in Fig. 5 *A* and *B*). However, the peaked DOS at the Fermi surface in the paramagnetic phase shifts downward (arrows in Fig. 5 *A* and *B*), indicating the removal of electronic states and the creation of a band gap.

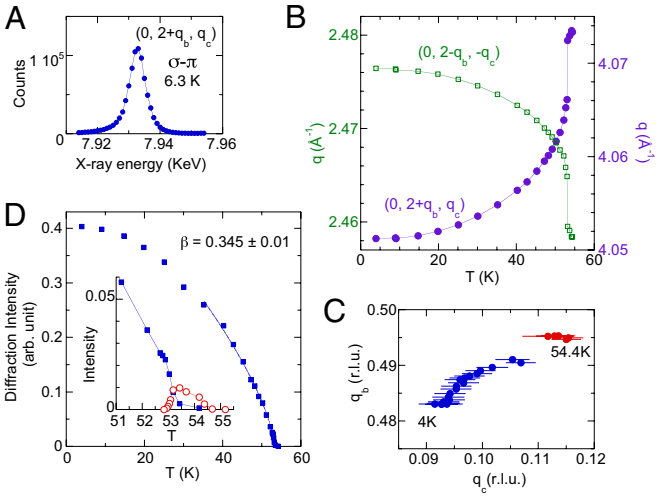

Fig. 3. Incommensurate antiferromagnetism in GdSi. (*A*) X-ray energy dependence of resonant magnetic scattering at the Gd *L*2 edge. (*B*) Measured *q* values of (0, $2\pm q_b$, $\pm q_c$) as a function of temperature from 4.0 to 54.4 K. (*C*) Temperature trajectory of Q = (0, q_b, q_c) in the *K*–*L* plane. (*D*) Order parameter of the magnetic phase measured as a sum of diffraction intensities at (0, $2\pm q_b$, $\pm q_c$) and azimuthal angle $\varphi = 0$, and normalized by that of (0, 2, 0). The order parameter has a small discontinuity at T_{SF} = 53.0 K (*Inset*), together with phase coexistence typical of a first-order transition in a small temperature range around T_{SF}. The high-temperature magnetic phase (red, *Inset*) shows a second-order transition at T_N. The intensity of the low-temperature phase (blue) is fit to a power-law form near the transition with a critical exponent β. Because the diffraction intensity *I* varies with the average staggered magnetic moment *m* as $I \sim m^2$, the order parameter of the low-temperature phase is fit with a power law as $I \sim (T_{SF} - T)^{2\beta}$ for $(1-T/T_{SF}) <$ 0.34 near the phase boundary. We obtain a value of $\beta = 0.345 \pm 0.010$ that is consistent with critical exponents of many Gd-based antiferromagnets such as $GdCo_2Ge_2$ (7), and is typical of isotropic Heisenberg spin fluctuations in three dimensions. The fit also gives a projected T_{SF} = 53.35 K, about 0.35 K above the cutoff temperature T_{SF} at the first-order transition.

PHYSICS

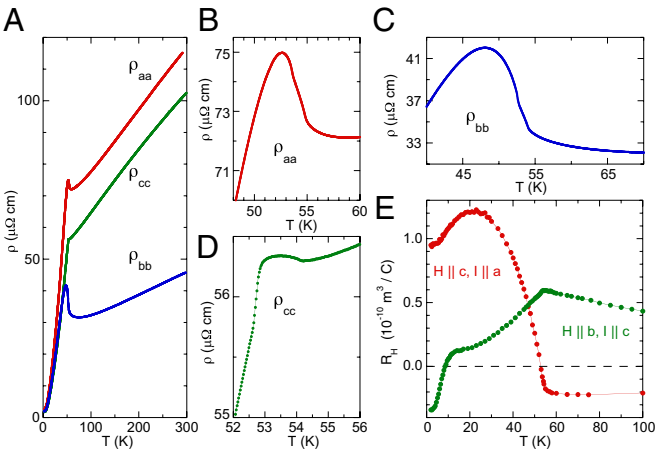

Fig. 4. Band gap opening at the antiferromagnetic transition. (*A*) Resistivity of GdSi measured along individual major axes with detailed view (*B–D*) around the transition regions. Both magnetic transitions and the loss of carriers (increasing resistivity with gap formation) have electronic signatures. (*E*) Hall coefficients measured for two field/current configurations, with a band crossing where the coefficient changes sign.

Signs of a Low-Dimensional, Nesting Fermi Surface. Having observed a connection between the formation of the incommensurate spin structure and the opening of a gap at the Fermi surface, the question naturally arises whether a nesting instability of the paramagnetic Fermi surface of GdSi may be responsible for the formation of a SDW among its itinerant electrons. However, neither the incommensurate spin structure nor the creation of band gap at the magnetic transition necessarily implies the presence of a nested Fermi surface. RKKY interactions between local moments alone could induce an incommensurate spin structure, as the associated superzone boundary may or may not intersect the paramagnetic Fermi surfaces to create a gap (15). The latter situation is exemplified in systems such as $GdNi_2Ge_2$ and $GdNi_2B_2C$ (21, 22). On the other hand, if perfectly nested portions of the paramagnetic Fermi surface are present in GdSi, the itinerant electrons will be susceptible to the formation of a SDW, which could in turn induce the incommensurate order of the local moments. For direct proof of a nesting condition, a direct probe of the Fermi surface such as ARPES (20) is necessary. In the absence of such data, we resort instead to both band structure calculation and indirect evidence obtained in the bulk-sensitive X-ray diffraction measurement of the magnetic Bragg peak line shape near the second-order phase boundary at T_N. According to the unpolarized band structure calculation, there are several Fermi surface sheets and the dominant band is shown in Fig. 5*A*, *Inset*. (The full results are presented in *SI Text*.) This band shows good nesting features at approximately the correct wave vector for the antiferromagnetic instability seen in experiment. Our experimentally measured asymmetric line shapes also establish that the itinerant states participating in the magnetic ordering exist on low-dimensional Fermi surface sheets that are necessarily nested.

The cross-section of elastic X-ray magnetic scattering is proportional to the static form factor $S(q,\omega=0)=\int e^{iqx}\langle s(x,t)s(0,0)\rangle dxdt$, which is equivalent to the thermal ensemble average $S(q)=\int e^{iqx}\langle s(x,0)s(0,0)\rangle_{KT}dx$ of the instantaneous (equal-time) spin-density–spin-density correlation function (9, 27). The form factor is related to the spin susceptibility through the fluctuation–dissipation theorem $S(q,\omega=0)\propto\lim_{\omega\to 0}\chi''(q,\omega)/\omega$, where $\chi''(q,\omega)$ is the imaginary part of the spin susceptibility (30). $\chi''(q,\omega)$ with a nonzero ω is often evaluated through inelastic neutron scattering (31), whereas $\chi''(q,0)$ is readily probed by elastic X-ray scattering. Even for noninteracting electrons, when $\chi(q,\omega)$ is given by the well-known Lindhard function, the susceptibility has different characteristic forms in one, two, and three dimensions (32). Because the spin susceptibility is directly related to the magnetic diffraction line shape, we can use the latter to determine the effective dimensionality of the Fermi surface states giving rise to the diffraction peak. With the current resonant magnetic scattering condition where the resonance is of the electric dipole $E1$ type (27), the cross-section is dominated by itinerant Gd 5*d* states. Hence, the measured line shape primarily reflects the dimensionality of the itinerant electron states that become gapped at the onset of the magnetic order.

We plot in Fig. 6 line shapes of the incommensurate magnetic order in GdSi at several temperatures just below T_N. At the relatively low temperature of 52 K, elastic magnetic peaks $(0, 2\pm q_b, \pm q_c)$ and lattice peak (0, 2, 0) all have an instrument resolution limited width and a line shape best described by the symmetric pseudo-Voigt function. At 53.7 and 54.2 K, the magnetic line shapes gradually become asymmetric, mirroring each other relative to the (0, 2, 0) order, whereas the (0, 2, 0) lattice peak remains symmetric and identical to that at lower temperature. This rules out lattice strain as a cause of asymmetry in magnetic diffraction peaks. We interpret the asymmetric peak shape as direct evidence of the presence of low-dimensional portions of Fermi surface. Similar asymmetry is also observed in Cr (28), which is considered an archetypical example of a nesting-driven SDW (14). In Cr, all 3*d* spins are itinerant with no local moments and the asymmetric line shapes near the thermal phase boundary were attributed to imperfect nesting conditions at the Fermi surface (28), in close analogy to the asymmetry caused by the presence of low-dimensional portions of Fermi surface discussed here (32).

The observed asymmetric line shapes in Fig. 6 can be compared with analytical forms of the Lindhard function in various dimensions. For free itinerant electrons, the Lindhard function in two dimensions is proportional to $\Theta(2k_F-q)/\sqrt{2k_F-q}$ in the vicinity of $q=2k_F$, whereas it is a step function in three dimensions and a delta function in one dimension (32). Convolving the 2D functional form with our instrument resolution, as exemplified by the (0, 2, 0) lattice peak, the resulting curve is plotted in Fig. 6, together with resonant scattering data at 54.2 K. We observe

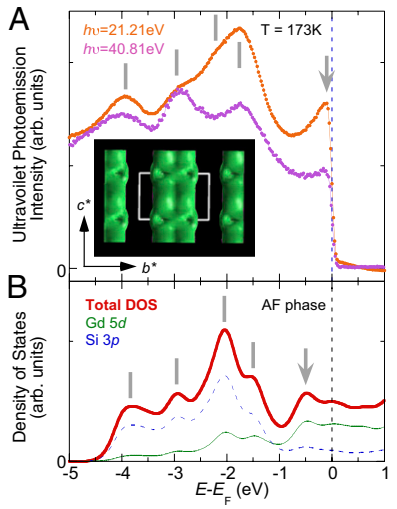

Fig. 5. DOS at the Fermi surface. (*A*) UV photoemission spectra measured at two incident energies. The photoemission data have spectral features of the valence bands marked by gray vertical bars. (*Inset*) A dominant band at the Fermi surface is shown from the band structure calculation. Calculated unpolarized bands are contaminated by unphysical weight from the Gd *f* states near the Fermi surface, but the band shown here is predominantly of Si character. (*B*) Calculated DOS results for the antiferromagnetic phase. The spectrum is composed of contributions from subbands, of which only the Gd 5*d* and Si 3*p* contribute significantly. Vertical bars indicate corresponding spectral features, whereas the arrows indicate a shift of DOS from the Fermi surface in the antiferromagnetic phase, with the creation of a band gap.

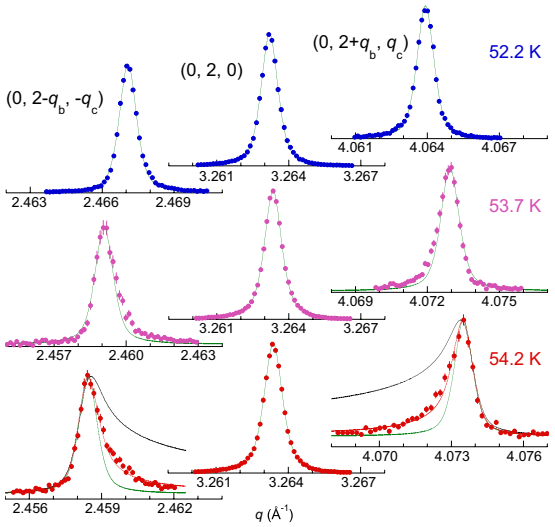

Fig. 6. Signatures of a low-dimensional Fermi surface. Single-crystal longitudinal diffraction line shapes of magnetic orders (0, 2±q_b, ±q_c) compared with that of lattice order (0, 2, 0) for three temperatures close to T_N. Solid lines are various fits to the data with pseudo-Voigt form as the instrument resolution (green); asymmetric function $\Theta(2k_F-q)/\sqrt{2k_F-q}$ convoluted with instrument resolution (black); and asymmetric function $\Theta(2k_F-q)/|2k_F-q|$ convoluted with instrument resolution (red). All data were measured in the σ-π geometry of X-ray polarization with no background subtracted and horizontal axes marking the zero level of intensity. Vertical error bars represent 1σ counting statistics.

that the experimental result shares the characteristic asymmetry of the Lindhard function, but is steeper than the standard 2D function and best approximated by $\Theta(2k_F-q)/|2k_F-q|$, indicating that it lies between the square-root divergence of the perfectly 2D case and the delta function form of the perfectly 1D Fermi surface. We conclude that there are quasi–1D, sheet-like portions of the Fermi surface for those itinerant Gd 5*d* electrons that are related to the magnetic ordering. Such sheet-like structures necessarily imply at least an imperfect nesting condition and the presence of a corresponding tendency toward the formation of a SDW.

Discussion

A number of transition-metal and rare-earth intermetallics incorporate both local moment and RKKY physics. In CeGe, although the exact nature of the magnetic ordering remains unknown, resistance anomalies were observed along all three major axes in single-crystal samples, indicating the opening of a band gap with incipient antiferromagnetic order (33). For CeSi, neutron powder diffraction results (34) established an incommensurate antiferromagnetic ground state close to (0, 0.5, 1/16) that is similar to what we found for GdSi. The local moment varies vastly from Ce (1.67 μ_B) (34) to Gd (8.4 μ_B) (24), yet the conduction bands are similar, with $5d^16s^2$ states from either Ce or Gd, and s^2p^2 states from either Si or Ge. We therefore suggest that the RKKY interaction between local moments is unlikely to be solely responsible for antiferromagnetic states with such similar wave vectors. Instead, we propose that the band structure, which is determined by both crystalline symmetry and valence states, and which is similar for GdSi, CeGe, and CeSi, is likely to play an important role in dictating the wave vector of the magnetic order through its partially nested Fermi surface.

Other FeB-structured RSi antiferromagnets (R = Tb, Dy, Ho) have similar magnetic order around (0, 0.5, q_c) at elevated temperatures (35). In these systems, the sizes of the local moments are similar to Gd, but the valence bands are significantly different from that of GdSi, with no 5*d* electron contribution from rare-earth ions. This indicates that even in the absence of nested itinerant spins, RKKY interactions are strong enough to stabilize a magnetically ordered phase. The whole series of FeB-structured rare-earth monosilicide/germanide could represent an elegant chemical tuning of the relative strengths of nesting-driven and RKKY-based incommensurate antiferromagnetic order, by replacement of various magnetic and nonmagnetic species in the stoichiometric structure.

The interplay between a nesting-induced itinerant SDW and the RKKY-ordered local moments can be understood on the microscopic level by considering the usual interaction Hamiltonian (36):

$$H_{int} = \frac{V}{N}\sum_{k,s,S,j} e^{i(k-k')j} c^+_{ks}\hat{\sigma}_{ss'}c_{k's'}d^+_{jS}\hat{\sigma}_{SS'}d_{jS'}. \quad [1]$$

Operators c^+_{ks} and d^+_{jS} create an itinerant electron with momentum k and spin s, and a local moment S at site j, respectively, coupled together by Pauli matrices $\hat{\sigma}_{ss'}$. This Hamiltonian can be approached from two different perspectives. First, integrating out the itinerant electron degrees of freedom with second-order perturbation theory gives the effective RKKY interaction between local moments $\vec{S}_j$ on site j as $H_{local} = \sum_q \sum_{j,j'} J(q) e^{iq(j-j')}\vec{S}_j\vec{S}_{j'}$. The q dependence of the magnetic interaction strength $J(q)$ is determined by the magnetic susceptibility $\chi(q)$, which under the random phase approximation is constructed out of the bare susceptibility $\chi_0(q)$ and the effective interaction U of itinerant electrons as $\chi(q) = \chi_0(q)/(1-U\chi_0(q))$. If the Fermi surface is nested, $\chi_0(q)$ will be enhanced at the corresponding wave vector and consequently the local moments will preferentially order at that wave vector. In addition, $\chi(q)$ would predominantly reflect the enhancement of $\chi_0(q)$ near the transition, as testified to by our observed line shapes. Conversely, one could take the mean-field expectation value for local moments in Eq. **1**, yielding a coupling between itinerant electrons in the form $H_{itinerant} = \sum_{k,k',s,s'} V(k-k',s,s') c^+_{ks}c_{k's'}$. In this approach, the interaction $V(k\text{-}k')$ would peak at the wave vector of the local moments' order, and in the presence of nesting it is responsible for opening a SDW gap at the Fermi surface (13). This situation is in fact precisely analogous to the Peierls transition in CDW systems, where ordered displacements of local ionic cores stabilize the emergence of a CDW in a partially nested material (25).

GdSi represents a system in which nesting and RKKY interactions have comparable strengths, and self-consistently cooperate to form an incommensurate antiferromagnetic ground state. Itinerant electrons dictate the ordering wave vector from the nesting condition, which constrains the broad q range favored by the RKKY interaction between local moments. In a self-consistent manner, the itinerant SDW order aligns local moments, and at the same time the scattering of itinerant electrons from the local magnetic order provides the necessary coupling strength between nested portions of the Fermi surface to create a SDW at the same wave vector. Thus, the incommensurate spin structure in GdSi serves as a clean model system to study the delicate interactions of itinerant and local electron spins, but is also minimally affected by further complications of orbital and lattice couplings. As we demonstrate here, this makes the binary system very accessible for theoretical modeling. Other similarly structured rare-earth monosilicides and germanides are ripe for comparison once they are available in single-crystal form. In addition to chemical tuning with various rare-earth elements, pressure and magnetic field would be powerful tools to regulate the incommensurate spin structure.

Methods

Sample Preparation. GdSi single crystals ~4 mm in diameter and ~70 mm in length were grown under a purified Ar atmosphere by the floating zone technique (24). Diffraction patterns collected on pulverized single crystals at 300 K confirmed that GdSi crystals are single phase. Elemental analysis of the crystals confirmed the stoichiometric Gd:Si ratio. X-ray Laue imaging was used to orient the crystals with an accuracy of 1°. Crystals were cut to size using either an acid saw or electrical discharge machining. All samples

surfaces were polished to a mirror finish with 0.05-μm alumina suspension (Buehler).

X-Ray Diffraction. Single-crystal X-ray diffraction was performed at Sector 4-ID-D of the Advanced Photon Source (APS) using the vertical diffraction geometry. For line shape studies, a reciprocal-space longitudinal resolution better than 1×10^{-3} Å^{-1} FWHM can be achieved with detector slits of 1×0.1 (H × V) mm^2 placed 1.3 m away from the sample. Resonant magnetic diffraction used 7,933 eV X-rays at the Gd *L2* edge using a plate sample in the Bragg geometry and a matching graphite (0, 0, 6) polarization analyzer fixed in the σ–π geometry. Our observed line shapes correspond solely to the elastic process in $S(q, \omega = 0)$ because the inelastic X-ray scattering is much weaker than the elastic process, and being incoherent does not constructively interfere. The inelastic process also would not change the polarization of the X-rays. Hence, although the NaI X-ray detector does not have good energy sensitivity, both the narrow detector slit setting and the σ–π scattering geometry make the contribution from inelastic scattering negligible. For lattice studies, nonresonant X-ray diffraction at 20.000 keV was performed in the Laue geometry on a 50-μm-thick sample with 0.04° mosaicity. Both incident beams were focused to a FWHM size of 250×120 (H × V) μm^2 and attenuated by a factor of ~8–10 throughout to avoid sample heating. The diffracted intensities were confirmed to vary linearly with incident X-ray intensity near the phase boundary. A Gifford–MacMahon-type cryostat provided sample temperature down to 4.0 K with a thermal stability of ± 0.02 K. High-resolution X-ray powder diffraction was performed at Sector 11-BM of APS, with an analyzer-based detector array of ~1.5×10^{-3} Å^{-1} FWHM resolution at 33.5 keV. Measurements were performed at 60 and 6.6 K, with the high-temperature phase of GdSi found to be consistent with the Pnma space group reported in the literature.

Magnetotransport. Four-probe resistivity measurements were made using bar-shaped single-crystal samples of typical size $(2 \times 0.4 \times 0.05)$ mm^3, aligned to under 5° along the three principal crystal axes at Sector 6-ID-D of APS. Hall effect measurements were made on similarly sized 5-probe Hall bars laser-cut from aligned single crystals, over a field range of ±5,000 Oe. Resistivity and Hall coefficients were measured using an LR700 resistance bridge in a Quantum Design physical property measurement system (PPMS) to $T = 2.0$ K, with a systematic error of ±5% due to uncertainties in dimensions. DC magnetic susceptibilities were measured for $1.8 < T < 300$ K along all three major axes using a Quantum Design magnetic property measurement system (MPMS) in a 160-Oe probe field.

UV Photoemission Spectroscopy. UV photoemission spectra were recorded with a resolution of 28.5 meV using a Perkin-Elmer/Physical Electronics model 5600 electron spectroscopy for chemical analysis (ESCA) system equipped with a SPECS UVS 300 UV lamp (He-I, $h\nu$=21.21 eV; He-II, $h\nu = 40.81$ eV), and a spherical capacitor analyzer (37). A GdSi sample with *b*-axis surface normal was held at 173 K for the measurement, after repeated surface treatment cycles of Ar ion sputtering and annealing at 923 K.

Band Structure Calculations. First-principles band structure calculations were performed using the generalized gradient approximation (GGA)+U approach in the full-potential linearized-augmented-plane-wave method (ref. 38 and references therein), where U is the Hubbard correlation term. The DOS in the antiferromagnetic phase is calculated for a spin structure with a (0, 1/2, 0) wave vector, which doubles the lattice size along the *b* axis, in an approximation of the incommensurate wave vector in the real system.

ACKNOWLEDGMENTS. We thank H. Li for assistance in sample preparation; D. Robinson and M. Suchomel for assistance in X-ray diffraction at Sectors 6-ID-D and 11-BM of APS, respectively; and J. A. Aguilar, J. C. Lashley, and J. L. Smith for helpful conversations. The work at The University of Chicago was supported by National Science Foundation (NSF) Grant DMR-1206519 and used Materials Research Science and Engineering Centers shared facilities, NSF Grant DMR-0820054. The work at the APS and the Materials Science Division of Argonne National Laboratory was supported by US Department of Energy-Basic Energy Science (DOE-BES) under Contract NEAC02-06CH11357. P.B.L. was supported by DOE-BES under FWP70069. B.M. and R.K.S. were supported in part by the US DOE under the Los Alamos National Laboratory-Lab Director Research and Development program. Work at Oak Ridge National Laboratory was supported by the Materials Sciences and Technology Division, DOE-BES. A.P. is supported in part by DOE-SCGF under Contract DE-AC05-06OR23100.

1. Tranquada JM, Sternlieb BJ, Axe JD, Nakamura Y, Uchida S (1995) Evidence for stripe correlations of spins and holes in copper oxide superconductors. *Nature* 375(6532): 561–563.
2. Hayden SM, Mook HA, Dai P, Perring TG, Doğan F (2004) The structure of the high-energy spin excitations in a high-transition-temperature superconductor. *Nature* 429(6991):531–534.
3. Ishikawa Y, Tajima K, Bloch D, Roth M (1976) Helical spin structure in manganese silicide MnSi. *Solid State Commun* 19(6):525–528.
4. Fawcett E (1988) Spin-density-wave antiferromagnetism in chromium. *Rev Mod Phys* 60(1):209–283.
5. Jensen J, Mackintosh AR (1991) *Rare Earth Magnetism* (Clarendon, Oxford).
6. Detlefs C, et al. (1996) Magnetic structure of $GdNi_2B_2C$ by resonant and nonresonant x-ray scattering. *Phys Rev B* 53(10):6355–6361.
7. Good W, et al. (2005) Magnetic structure of $GdCo_2Ge_2$. *Phys Rev B* 71(22):224427.
8. Lee HNS, McKinzie H, Tannhauser DS, Wold A (1969) The low-temperature transport properties of $NbSe_2$. *J Appl Phys* 40(2):602–604.
9. Feng Y, et al. (2012) Order parameter fluctuations at a buried quantum critical point. *Proc Natl Acad Sci USA* 109(19):7224–7229.
10. Kimura T, et al. (2003) Magnetic control of ferroelectric polarization. *Nature* 426(6962):55–58.
11. Milward GC, Calderón MJ, Littlewood PB (2005) Electronically soft phases in manganites. *Nature* 433(7026):607–610.
12. Jaramillo R, Feng Y, Wang J, Rosenbaum TF (2010) Signatures of quantum criticality in pure Cr at high pressure. *Proc Natl Acad Sci USA* 107(31):13631–13635.
13. Overhauser AW (1962) Spin density waves in an electron gas. *Phys Rev* 128(3): 1437–1452.
14. Norman MR, Si Q, Bazaliy YB, Ramazashvili R (2003) Hall effect in nested antiferromagnets near the quantum critical point. *Phys Rev Lett* 90(11):116601.
15. Elliott RJ, Wedgwood FA (1963) Theory of the resistance of the rare earth metals. *Proc Phys Soc* 81(5):846–855.
16. Elliott RJ (1965) *Magnetism Vol. IIA*, eds Rado GT, Suhl H (Academic, London), pp 385–424.
17. Overhauser AW (1963) Spin-density-wave mechanisms of antiferromagnetism. *J Appl Phys* 34(4):1019–1024.
18. Schiffer P, et al. (1995) Frustration induced spin freezing in a site-ordered magnet: Gadolinium gallium garnet. *Phys Rev Lett* 74(12):2379–2382.
19. Islam Z, et al. (1999) Effects of band filling on magnetic structures: The case of RNi_2Ge_2. *Phys Rev Lett* 83(14):2817–2820.
20. Inosov DS, et al. (2009) Electronic structure and nesting-driven enhancement of the RKKY interaction at the magnetic ordering propagation vector in Gd_2PdSi_3 and Tb_2PdSi_3. *Phys Rev Lett* 102(4):046401.
21. Bud'ko SL, et al. (1999) Anisotropy and metamagnetism in the RNi_2Ge_2 (R=Y, La-Nd, Sm-Lu) series. *J Magn Magn Mater* 205(1):53–78.
22. Hennings BD, Naugle DG, Canfield PC (2002) Thermal transport of the single-crystal rare-earth nickel borocarbides RNi_2B_2C. *Phys Rev B* 66(21):214512.
23. Saito H, Suzuki S, Fukamichi K, Mitamura H, Goto T (1996) Metamagnetic transition in GdSi. *J Phys Soc Jpn* 65(7):1938–1940.
24. Tung LD, et al. (2005) Field-induced magnetic phase transitions in a GdSi single crystal. *Phys Rev B* 71(14):144410.
25. Peierls RE (1955) *Quantum Theory of Solids* (Oxford Univ Press, Oxford), p 108.
26. Nagaki DA, Simon A (1990) Structure of gadolinium monosilicide. *Acta Crystallogr C* 46(7):1197–1199.
27. Hill JP, McMorrow DF (1996) X-ray resonant exchange scattering: polarization dependence and correlation functions. *Acta Crystallogr A* 52(2):236–244.
28. Jaramillo R, et al. (2008) Chromium at high pressures: Weak coupling and strong fluctuations in an itinerant antiferromagnet. *Phys Rev B* 77(18):184418.
29. Schmiedeshoff GM, et al. (2004) Magnetotransport and superconductivity of α-uranium. *Philos Mag* 84(19):2001–2022.
30. Plischke M, Bergersen B (2006) *Equilibrium Statistical Physics* (World Scientific, Singapore), 3rd ed.
31. Schröder A, et al.; v. Lohneysen H (2000) Onset of antiferromagnetism in heavy-fermion metals. *Nature* 407(6802):351–355.
32. Littlewood PB (1994) Spin fluctuations in a two-dimensional marginal Fermi liquid. *J. Supercond* 7(3):511–515.
33. Das PK, Kumar N, Kulkarni R, Dhar SK, Thamizhavel A (2012) Anisotropic magnetic properties and superzone gap formation in CeGe single crystal. *J Phys Condens Matter* 24(14):146003.
34. Schobinger-Papamantellos P, Buschow KJ (1994) Incommensurate magnetic structure of CeSi as observed by neutron diffraction. *J Magn Magn Mater* 130(1–3):242–246.
35. Schobinger-Papamantellos P, Buschow KJ, Rodríguez-Cavajal J (2011) Magnetic phase diagrams of the CrB- and FeB-type HoSi compounds. *J Magn Magn Mater* 323(21): 2592–2607.
36. Van Vleck JH (1962) Note on the Interaction between the spins of magnetic ions or nuclei in metals. *Rev Mod Phys* 34(4):681–686.
37. Opeil CP, et al. (2006) Valence-band UPS, 6*p* core-level XPS, and LEED of a uranium (001) single crystal. *Phys Rev B* 73(16):165109.
38. Blaha P, Schwarz K, Madsen GKH, Kvasnicka D, Luitz J (2001) *WIEN2K, An Augmented Plane Wave Plus Local Orbitals Program for Calculating Crystal Properties* (Technische Universität Wien, Vienna, Austria).